Moiré edge states in twisted bilayer graphene and their topological relation to quantum pumping

Manato Fujimoto and Mikito Koshino

Phys. Rev. B **103**, 155410 — Published 12 April 2021

DOI: 10.1103/PhysRevB.103.155410

Moiré edge states in twisted bilayer graphene and their topological relation to quantum pumping

Manato Fujimoto[1] and Mikito Koshino[1]

[1] *Department of Physics, Osaka University, Osaka 560-0043, Japan*

(Dated: March 30, 2021)

We study the edge states of twisted bilayer graphene and their topological origin. We show that the twisted bilayer graphene has special edge states associated with the moiré pattern, and the emergence of these moiré edge states is linked with the sliding Chern number, which describes topological charge pumping caused by relative interlayer sliding. When one layer of the twisted bilayer is relatively slid with respect to the other layer, the edge states are transferred from a single band to another across the band gap, and the number of the edge states pumped in a sliding cycle is shown to be equal to the sliding Chern number of the band gap. The relationship can be viewed as a manifestation of the bulk-edge correspondence inherent in moiré bilayer systems.

I. INTRODUCTION

In condensed matter systems, the topology of electronic band is intimately related to the emergence of edge states, i.e., electronic states localized at the boundary of the system.[1–3] In general, the existence of edge states in a specific band gap is related to the non-zero topological invariant in the bulk system.[4,5] In quantum Hall systems, for example, the number of edge modes coincides with the summation of the Chern numbers over all the occupied bands below the gap.[1,4–6] Similar relationships between bulk topological property and emergent edge modes are found in a wide variety of physical systems, including topological insulators, topological superconductors,[7,8] mechanical systems[9–11] and photonic systems.[12,13]

In this paper, we study the edge states of twisted bilayer graphenes (TBG) and their topological origin. TBG is a two-dimensional material where two graphene layers are overlapped with an arbitrary twist angle. In a low-angle TBG, the long-range moiré pattern strongly modifies the graphene's Dirac cone[14–25], resulting in a flat band at zero energy.[19,24,26,27] Some previous works studied the edge properties of TBG,[28–33] and it was shown that TBG has two kinds of the edge states[32]: One is zero-energy edge modes on the zigzag termination[28–31], which are inherited from monolayer graphene.[34] The other one, which we refer to moiré edge state, is qualitatively different state strongly dependent on the moiré pattern, and occurs away from zero energy.[32,33] Around the magic angle, in particular, the moiré edge states come to the energy gaps between flat band and excited band.[33]

One may ask if the moiré edge states are related to some sort of bulk topology. The energy bands of TBG has zero Chern number, and hence the system does not have any edge states associated with the Hall effect or the valley Hall effect. Recent works[35–37] proposed a different topological invariant for TBG, called sliding Chern number, which represents the number of adiabatic charge pumping[38] caused by a mechanical interlayer sliding. More specifically, when one layer of TBG is relatively slid with respect to the other layer by a single atomic period, then electrons on the TBG are pumped by an integer multiple of the moiré period, where the integer is given by the sliding Chern number.

Here we investigate the edge states of TBG under the effect of the interlayer sliding, and find that the emergence of the moiré edge states is linked with the nonzero sliding Chern numbers. We demonstrate that the edge states are transferred in the energy axis from the flat band to the excited band during the interlayer sliding process, and the number of edge states pumped in a sliding cycle is equal to the sliding Chern number of the band gap. The relationship can be viewed as a bulk-edge correspondence inherent in moiré bilayer systems.

The paper is organized as follows. In Sec. II, we introduce the atomic structure of TBG and the tight binding model. In Sec. III, we calculate the energy spectrum of TBG nanoribbon as a function of sliding distance, and demonstrate the correspondence between the edge states and the sliding Chern number. A brief conclusion is given in Sec. IV.

II. MODEL

A. Atomic structure

TBG can be generated from AA-stacked bilayer graphene (i.e., perfectly overlapping honeycomb lattices) by rotating layer 1 and 2 by $-\theta/2$ and $\theta/2$, respectively. Figure 1 illustrates the atomic struc-

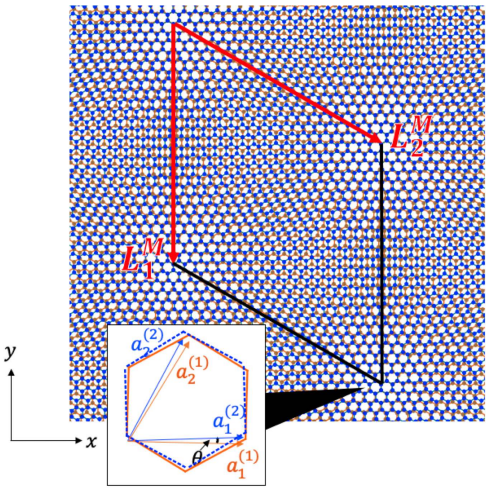

FIG. 1. Atomic structures and the moiré unit cell of TBG with $\theta = 2.65°$. The inset shows the primitive lattice vectors of layers 1 and 2.

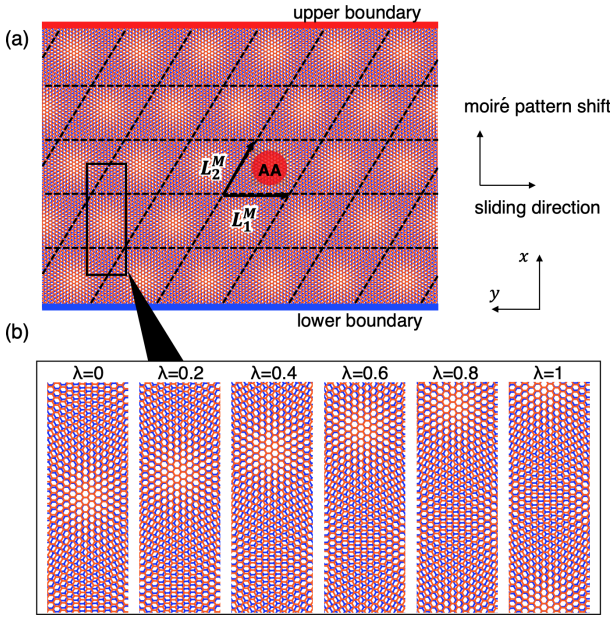

FIG. 2. (a) TBG nanoribbon with 2.65° truncated by upper (red) and lower (blue) boundaries. Note that the figure is rotated by 90° so that x axis is vertical and y axis is horizontal. The structure is periodic in the direction of $\mathbf{L}_1^M$, and five unit cells thick in the perpendicular direction. (b) Detailed atomic structure in the sliding parameter $\lambda = 0, 0.2, ..., 1$.

ture of TBG of 2.65°. We define $\mathbf{a}_1 = a(1,0), \mathbf{a}_2 = a(1/2, \sqrt{3}/2)$ as the lattice vectors of monolayer graphene before the rotation, where $a = 0.246$nm is graphene's lattice constant. The lattice vectors of layer l after the rotation are given by $\mathbf{a}_i^{(l)} = R(\mp\theta/2)\mathbf{a}_i$ with $\mp$ for $l = 1, 2$ respectively, where $R(\theta)$ represents the rotation by θ on xy-plane.

When the rotation angle is small, the mismatch between the lattice structures of the two layers gives rise to a long-range moiré pattern, which is ruled by the primitive lattice vectors,

$$\begin{aligned}\mathbf{L}_i^M &= [R(\theta/2) - R(-\theta/2)]^{-1}\mathbf{a}_i \quad (i = 1, 2) \\ &= \frac{1}{2\sin(\theta/2)} R(-\pi/2)\mathbf{a}_i, \end{aligned} \tag{1}$$

with $\mp$ for $l = 1, 2$. The lattice constant $L_M = |\mathbf{L}_1^M| = |\mathbf{L}_2^M|$ is given by

$$L_M = \frac{a}{2\sin(\theta/2)}. \tag{2}$$

If we slide the layer l by $\mathbf{a}_i^{(l)}$ with the other layer fixed, the moiré pattern shifts exactly by $\pm\mathbf{L}_i^M$ for $l = 1, 2$, respectively. Therefore, when we slide the layer l by an arbitrary displacement vector,

$$\Delta\mathbf{x}^{(l)} = \nu_1\mathbf{a}_1^{(l)} + \nu_2\mathbf{a}_2^{(l)}, \tag{3}$$

then the moiré pattern moves by

$$\begin{aligned}\Delta\mathbf{X} &= \pm(\nu_1\mathbf{L}_1^M + \nu_2\mathbf{L}_2^M) \\ &= \frac{\pm 1}{2\sin(\theta/2)} R(-\pi/2 \mp \theta/2)\Delta\mathbf{x}^{(l)}, \end{aligned} \tag{4}$$

where each double sign corresponds to $l = 1, 2$, respectively. When $\theta \ll 1$, the moiré pattern shift $\Delta\mathbf{X}$ is nearly perpendicular to the sliding vector $\Delta\mathbf{x}^{(l)}$, and its amplitude is magnified by the factor $[2\sin(\theta/2)]^{-1} \sim 1/\theta$.

In the following, we consider a TBG nanoribbon as shown in Fig. 2(a) to investigate the edge states. Note that the figure is rotated by 90° so that x axis is vertical and y axis is horizontal. Here we assume that the ribbon is parallel to y and five unit cells thick in the perpendicular direction (along x), truncated by red and blue lines. The boundary is nearly parallel to the armchair direction of graphene, so that the zigzag edge states of monolayer graphene are almost absent.

Now we slide layer 2 with respect to layer 1 in along the length of the ribbon (y), to move the moiré pattern along the width (x). We specify the sliding vector by $(\nu_1, \nu_2) = \lambda(1/2, -1)\,(0 \le \lambda \le 1)$, which gives $\Delta\mathbf{x}^{(2)}$ almost along $-y$ direction. When the sliding parameter λ is changed from 0 to 1, the moiré pattern moves by $\Delta\mathbf{X} = -(1/2)\mathbf{L}_1^M + \mathbf{L}_2^M$ exactly in the x-direction. After the process, all the AA spots move just by one row as illustrated in the

lower panel of Fig. 2(b). Because of the triangular-lattice arrangement, the AA spots of do not come back to the original positions, but as we will see, this process virtually gives a single cycle of the edge states pumping.

B. Tight binding model

We calculate the eigenenergies and the eigenfunctions of the TBG ribbon using the tight-binding model for carbon p_z orbitals. The Hamiltonian is written as[16,39–41]

$$H = -\sum_{\langle i,j\rangle} t\left(\mathbf{R}_i - \mathbf{R}_j\right) |\mathbf{R}_i\rangle \langle \mathbf{R}_j| + \text{H.c.} \qquad (5)$$

where $\mathbf{R}_i$ and $|\mathbf{R}_i\rangle$ represent the lattice point and the atomic state at site i, respectively, and $t\left(\mathbf{R}_i - \mathbf{R}_j\right)$ is the transfer integral between site i and site j. We adopt the Slater-Koster-type formula for the transfer integral,

$$\begin{aligned} -t(\mathbf{d}) &= V_{pp\pi}\left[1 - \left(\frac{\mathbf{d}\cdot\mathbf{e}_z}{d}\right)^2\right] + V_{pp\sigma}\left(\frac{\mathbf{d}\cdot\mathbf{e}_z}{d}\right)^2 \\ V_{pp\pi} &= V^0_{pp\pi}\exp\left(-\frac{d-a_0}{\delta_0}\right) \\ V_{pp\sigma} &= V^0_{pp\sigma}\exp\left(-\frac{d-d_0}{\delta_0}\right) \end{aligned} \quad , \qquad (6)$$

where $\mathbf{d} = \mathbf{R}_i - \mathbf{R}_j$ is the distance between two atoms, and $\mathbf{e}_z$ is the unit vector on the z axis. $V^0_{pp\pi}$ is the transfer integral between the nearest-neighbor atoms of monolayer graphene which are located at distance $a_0 = a/\sqrt{3} \approx 0.142$ nm. $V^0_{pp\sigma}$ is the transfer integral between two nearest vertically aligned atoms, $d_0 \approx 0.335$nm is the interlayer spacing. δ_0 is decay length of the transfer integral and is chosen as $0.184a$. The transfer integral for $d > \sqrt{3}a$ is exponentially small and can be safely neglected.

Our target is the TBG of the magic angle ($\theta = 1.05°$) which has nearly flat bands.[19,24,26,27,42–44] It has a huge number of atoms (about 12,000) in the moiré unit cell, requiring a large computational cost to calculate the energy bands of the ribbon which consists of multiple unit cells. To reduce the number of atoms, we take the atomic structure of $\theta = 2.65°$ which has 10 times fewer atoms per unit cell, but at the same time, enlarge the interlayer hopping energy (i.e., transfer integral between atoms of layer 1 and layer 2) by factor of $2.65°/1.05° \approx 2.52$, to mimic the band structure of $\theta = 1.05°$. The approximation works for the follow reason. The low-energy band structure of TBG is determined by the ratio of two energy scales, t_{inter}/E_M, where t_{inter} is the interlayer hopping energy, and $E_M = \hbar v(2\pi/L_M) \sim (2\pi\hbar v/a)\theta$ is the moiré band folding energy with graphene's band velocity v.[14,19,20,22,25,45–47] Therefore, the TBG of $\theta = 2.65°$ with t_{inter} multiplied by factor 2.52 has a nearly identical low-energy band structure as the original $\theta \sim 1.05°$ model except for the overall energy scale.

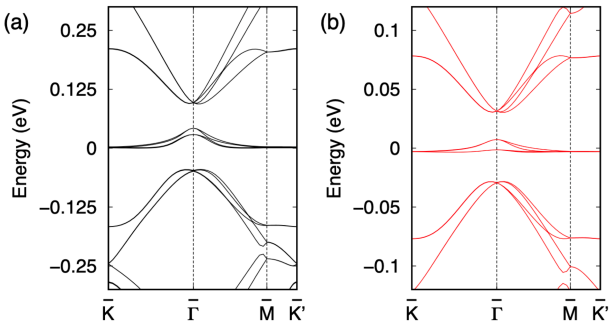

FIG. 3. Band structures of (a) $\theta = 2.65°$ tight-binding model with enlarged interlayer hopping by factor 2.52, and (b) of the original $\theta = 1.05°$ model (see the text).

Also, we include the in-plane lattice relaxation in the TBG atomic structure, which gives an energy gap between flat bands and the excited bands[43] (referred to as the moiré gap in the following). Here we set the lattice displacement vector $\mathbf{u}$ of $\theta = 1.05°$[43] in the lattice of 2.65° TBG, and construct the tight-binding Hamiltonian. The realistic TBG also has an out-plane relaxation[48–51], and it was shown to also contribute to opening the moiré gap in a similar manner[52–54]. Here we neglect the out-plane relaxation as it does not change the topology of the moiré gap opened by the in-plane relaxation.

Figure 3 plots the bulk band structure calculated for (a) the 2.65° model with three-times enlarged interlayer hopping, and (b) the original $\theta = 1.05°$ model, showing a quantitative agreement except for the energy scale difference by the factor about 2.52. In the following calculation, the energy scale is shrunk by 1/2.52 times to emulate 1.05° TBG. Note that the TBG of $\theta = 2.65°$ is a commensurate system at which the atomic structure is exactly periodic in the moiré period $\mathbf{L}_i^M$,[14,19,20,22,25,45–47] and hence the eigenstates of the tight-binding model can be obtained by diagonalizing a finite-sized Hamiltonian matrix.

III. RESULTS

A. Electronic structure and edge states

The calculated band diagram of the TBG ribbon is summarized in Fig. 4. Here Fig. 4(a) shows the band energies at the fixed wave number $k_y = \pi/L_1^M$, as a function of sliding parameter λ. The panel (b) presents the full band structure against k_y, at different sliding distances $\lambda = 0, 0.2, \cdots, 1$. In Fig. 4 (a) and (b), the colored lines are the energy bands of TBG ribbons, where the color represents the expected value of x coordinate; red (blue) lines indicate edge states localized at the upper (lower) boundary, while green lines are bulk states spreading over the entire system. The black-colored areas in background represent the energy bands of the bulk TBG projected onto k_y axis. Each of the edge states is an eigenstate of the time reversal operator, where the valley degree of freedom (K and K' in monolayer graphene) is mixed. At $\lambda = 0$, we have an additional in-plane C_2 symmetry, and there the edge states at upper and lower boundaries are force to degenerate, as seen in Fig. 4(a).

In increasing λ from 0 to 1, we see that two edge bands of the upper boundary (red lines) split off from the zero-energy flat band in each of positive and negative energy sides, and they are eventually absorbed into the excited conduction/valence bands. At the same time, two edge bands of the lower boundary (blue lines) transfer from the excited bands to the zero-energy band. The number shown on the right side of the Fig. 4(a) represent the number of pumped edge levels (per spin) across each energy gap. For example, '2' indicates that two upper-edge states goes up and two lower-edge states goes down in energy.

In Fig. 4(c), we present the squared wave function of the flat band states at $\bar{K}$ of a bulk TBG (not of the ribbon) at $\lambda = 0, 0.2, \cdots, 1$. Here the orange dots represent AA spots, and the red and blue lines represent the boundary lines for the ribbon. The wave amplitude is concentrated on the AA spots, which is a property of the flat band states[17,18,20,24]. In increasing λ, the bright spots on AA region shift upward to follow the moiré pattern movement. The emergence of the edge states correlates with the relative position of the AA spots to the boundary lines.[33] By comparing Figs. 4(a) and 4(c), we notice that two edge states of the top boundary (red curves) branch out from the zero-energy flat band right when the AA spots cross the boundary to the outside, and similarly, the two edge states of the lower boundary (blue curves) are absorbed into the flat band when the AA spots enter the ribbon from the lower boundary.

Figure 5 illustrates actual eigenstates of the TBG ribbon, (1), (2) and (3) at $\lambda = 0.3$, and (4), (5) and (6) at $\lambda = 0.7$, which are labelled in Fig. 4(a). We see that the in-gap states (1) and (2) are actually localized on the upper edge, and (4) and (5) are on the lower edge, while the bulk states (3) and (6) extend over the middle region.

B. Bulk edge correspondence

The number of edge states branching out or being absorbed per a sliding cycle ($0 \le \lambda \le 1$) exactly coincides with the sliding Chern number, which is a topological invariant defined for the Bloch bands of TBG[35–37]. Let us consider an infinite TBG and assume the Fermi energy lies in an energy gap. When we adiabatically slide the layer l by its own lattice period $\mathbf{a}_i^{(l)}$ with the other layer fixed, the change of electronic polarization is written as[35]

$$\Delta\mathbf{P} = C_{i1}^{(l)}\mathbf{L}_1^M + C_{i2}^{(l)}\mathbf{L}_2^M, \tag{7}$$

$$C_{ij}^{(l)} = \sum_{n=\text{occupied}} \int_0^1 dk_j \int_0^1 d\lambda_i \; i\left[\left\langle \frac{\partial u}{\partial \lambda_i}\middle|\frac{\partial u}{\partial k_j}\right\rangle - \left\langle \frac{\partial u}{\partial k_j}\middle|\frac{\partial u}{\partial \lambda_i}\right\rangle\right]. \tag{8}$$

Here $u = u_{n\mathbf{k}}(\lambda_1, \lambda_2)$ is the eigenstate of the n-th band at Bloch wave number $\mathbf{k}$, in the TBG Hamiltonian with the layer l shifted by $\lambda_1\mathbf{a}_1^{(l)} + \lambda_2\mathbf{a}_2^{(l)}$. The k_j is a dimensionless wave component defined by $\mathbf{k} = k_1\mathbf{G}_1^M + k_2\mathbf{G}_2^M$, where $\mathbf{G}_j^M$ is the moiré reciprocal lattice vector satisfying $\mathbf{G}_i^M \cdot \mathbf{L}_j^M = 2\pi\delta_{ij}$. $\mathbf{\Delta P}$ represents the shift of the polarization per a single moiré unit cell area during a sliding cycle. In the low twist-angle regime, particularly, the sliding Chern number can be defined for each of nearly-decoupled K and K' valleys independently, and the number does not depend on valley. Hence the total sliding Chern number is equal to twice that of a single valley. This can be verified by considering the time reversal symmetry in Eq. (8) (See, Appendix A).

When the Fermi energy is in the gap just above the flat band, the sliding Chern numbers per spin (summed over valleys) are calculated as $C_{11}^{(1)} = C_{22}^{(1)} = 2$, $C_{11}^{(2)} = C_{22}^{(2)} = -2$ and otherwise 0.[35] If we slide the layer 2 by $\Delta\mathbf{x}^{(2)} = (1/2)\mathbf{a}_1^{(2)} - \mathbf{a}_2^{(2)}$ as considered for the ribbon, the polarization shift per

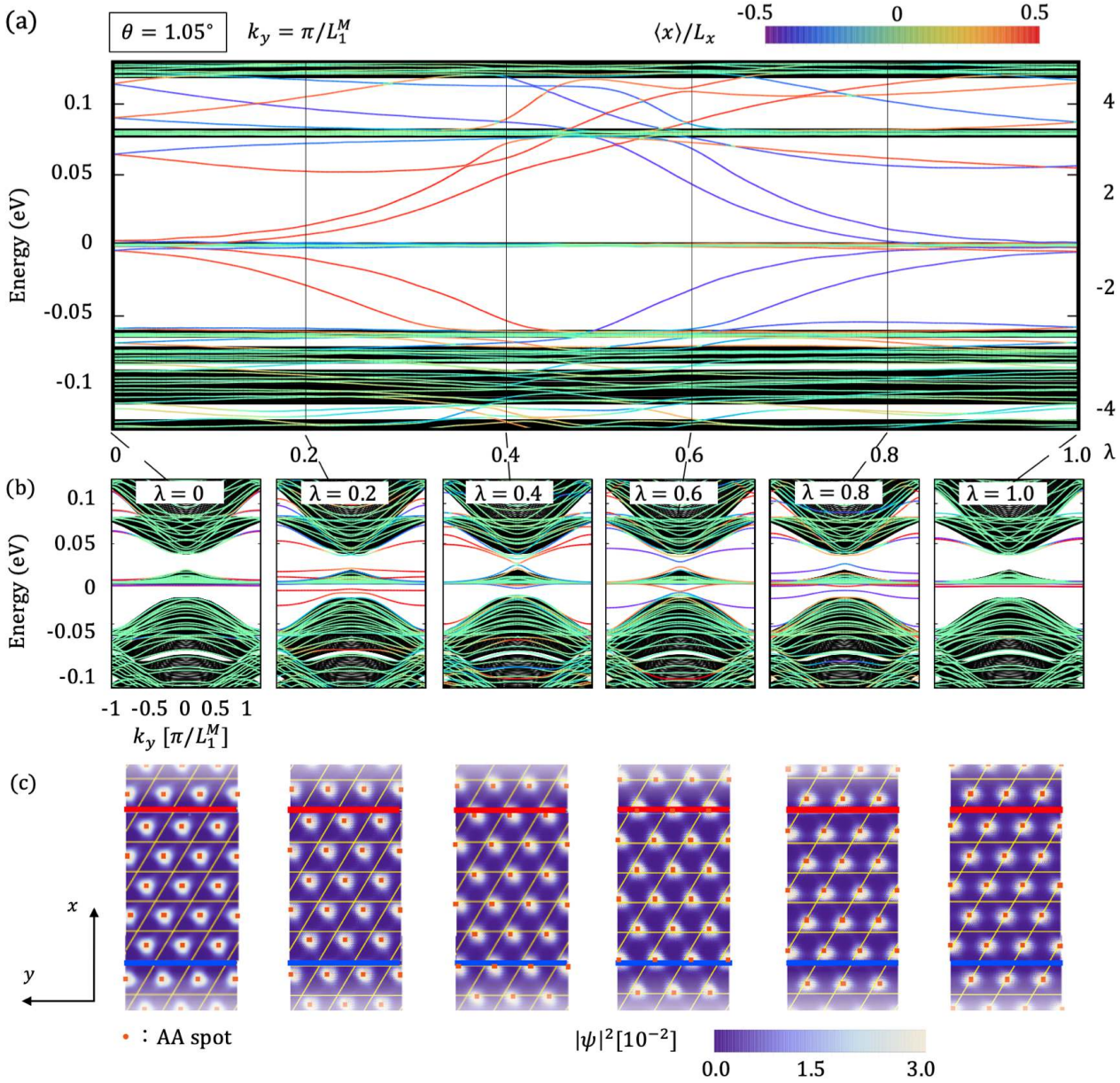

FIG. 4. (a) Energy band structure of TBG nanoribbon at $k_y = \pi/L_1^M$ as a function of sliding parameter λ, and (b) the full band structure against k_y at $\lambda = 0, 0.2, \cdots, 1$. Here the colored lines are the energy bands of TBG ribbons, where the color represents the expected value of x coordinate, and the black-colored areas in background represent the energy bands of the bulk TBG projected onto k_y axis. The numbers shown on the right side of the figure represent the number of pumped edge states (per spin) across the energy gap. (c) Real-space map of the flat-band wave function at $\bar{K}$ of bulk TBG at $\lambda = 0, 0.2, \cdots, 1$ [corresponding to upper panels in (b)]. The red and blue lines represent the boundary lines for the ribbon.

spin becomes

$$\Delta\mathbf{P} = \frac{1}{2}(C_{11}^{(2)}\mathbf{L}_1^M + C_{12}^{(2)}\mathbf{L}_2^M) - (C_{21}^{(2)}\mathbf{L}_1^M + C_{22}^{(2)}\mathbf{L}_2^M)$$
$$= 2\left(-\frac{1}{2}\mathbf{L}_1^M + \mathbf{L}_2^M\right) = 2\Delta\mathbf{X}, \quad (9)$$

where $\Delta\mathbf{X}$ is the shift of the moiré pattern argued in the previous section. This means that two electrons (per spin) pass through every unit-cell boundary perpendicular to x, and it perfectly corresponds

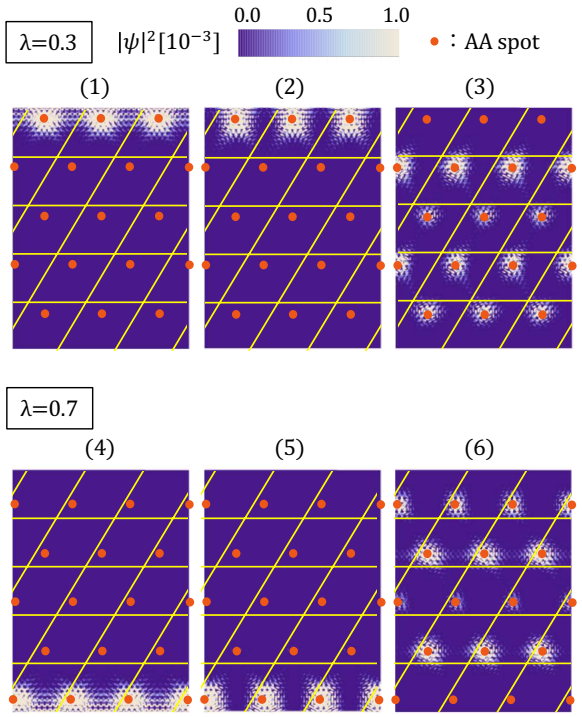

FIG. 5. Real-space map of low-energy eigenstates of the TBG ribbon. (1), (2) and (3) at $\lambda = 0.3$, and (4), (5) and (6) at $\lambda = 0.7$, which are labelled in Fig. 4(a).

the number of the edge states branching out from (or being absorbed to) the flat band per a sliding cycle, as argued in Fig. 4(a). The figure also shows that, in the second gap around 0.8 eV, four bands of the upper edge states go up, and four bands of the lower edge states go down in a sliding process from $\lambda = 0$ to 1. Correspondingly, the sliding Chern numbers (per spin) in the gap are $C_{11}^{(1)} = C_{22}^{(1)} = 4$, $C_{11}^{(2)} = C_{22}^{(2)} = -4$ and otherwise 0, giving $\mathbf{\Delta P} = 4\mathbf{\Delta X}$. The coincidence of the number of transferred edge states across the gap and the sliding Chern number can be viewed as a bulk edge correspondence in the moiré system. We note that the bulk-edge correspondence for the topological pumping was also proposed for a one-dimensional lattice with time-dependent moving potential.[55]

The edge state pumping and the bulk-edge correspondence in the moiré system are analogous to those in the quantum Hall effect (QHE).[4,5] In the quantum Hall system, a transfer of the edge states is observed against a change of the momentum along the Hall bar. In the moiré pumping, on the other hand, the edge state transfer occurs as a function as a sliding parameter λ, instead of the momentum. This corresponds to the fact that the conventional Chern number for the Hall conductivity σ_{xy} is an integral of the Berry curvature on the (k_x, k_y) space (torus), while the sliding Chern number, Eq. (8), is that on the (k_i, λ_j) space.

A notable difference from the QHE is that the sliding Chern number, Eq. (8), includes the momentum integration in only a single direction (the charge pumping direction), so that the momentum in the other direction remains as a parameter. In the case of Fig. 4, for example, the sliding Chern number is defined for each k_y, and it is topologically protected as long as the energy spectrum at the fixed k_y (and any k_x) is gapped. The bulk-edge correspondence stands at every single k_y, i.e., the sliding Chern number at given k_y corresponds to the number of the pumped edge levels at the k_y, as exactly observed in Fig. 4. In the QHE, in contrast, the Chern number includes the integral in both k_x, k_y, and it is well defined only when the spectrum is gapped on the entire two-dimensional momentum space of (k_x, k_y).

Since the number of transferred edge states during a sliding process is a topological invariant, it is expected to be robust even in the presence of the edge disorder. This can be intuitively understood as follows: During the interlayer sliding, the bulk state electrons are pumped towards the edge by the movement of the moiré pattern, and there must be in-gap edge states to absorb the excessive electrons accumulated at the edge regardless of the detailed edge structure.

While the above calculation is limited to the magic angle TBG, the pumping of the edge states occurs in a broad range of the twist angle. In Appendix B, we present the plots similar to Fig. 4 for $\theta = 1.47°, 2.65°$ and $6.01°$. In increasing the twist angle, we see that the moiré gap between the flat band and the excited band narrows and it partially closes in some region of k_y. But we still see the same number of the edge states pumped in the gapped region, because the sliding Chern number remains unchanged in the gap.

IV. CONCLUSION

We studied the edge states of TBG and the topological correspondence to relative interlayer sliding. By calculating the eigenfunctions of the edge-terminated TBG ribbon as a function of the sliding distance, we demonstrated that moiré edge states are transferred across the band gap during the interlayer sliding, and the number of edge states pumped in the sliding cycle coincides with the sliding Chern number

of the band gap. The relationship can be viewed as a manifestation of the bulk-edge correspondence in moiré bilayer systems, where nonzero sliding Chern number is always associated with the emergence of the moiré edge states.

The moiré charge pumping by interlayer sliding is expected also in other superlattices such as the graphene/hBN system[56–64] and twisted bilayers of transition metal diachalcogenides[65–70], whenever the Fermi energy is in an energy gap with non-zero sliding Chern number. Generally, the sliding Chern number can be non-zero in energy gaps opened by the superlattice interlayer interaction. Any gaps which already exists in monolayer are trivial in terms of the sliding Chern number, because the interlayer interaction can be continuously switched off without closing the gap, and then no moire pumping takes place. The moiré pumping in various van der Waals superlattices is left for future work.

ACKNOWLEDGMENTS

This work is supported by JSPS KAKENHI Grant Number JP20H01840 and JP20H00127, Japan, and by JST CREST Grant Number JPMJCR20T3, Japan.

[1] D. J. Thouless, M. Kohmoto, M. P. Nightingale, and M. den Nijs, Phys. Rev. Lett. **49**, 405 (1982).
[2] C. L. Kane and E. J. Mele, Physical review letters **95**, 146802 (2005).
[3] X.-L. Qi, T. L. Hughes, and S.-C. Zhang, Physical Review B **78**, 195424 (2008).
[4] Y. Hatsugai, Phys. Rev. Lett. **71**, 3697 (1993).
[5] Y. Hatsugai, Phys. Rev. B **48**, 11851 (1993).
[6] M. Kohmoto, Annals of Physics **160**, 343 (1985).
[7] M. Z. Hasan and C. L. Kane, Reviews of modern physics **82**, 3045 (2010).
[8] X.-L. Qi and S.-C. Zhang, Reviews of Modern Physics **83**, 1057 (2011).
[9] C. Kane and T. Lubensky, Nature Physics **10**, 39 (2014).
[10] T. Kariyado and Y. Hatsugai, Scientific reports **5**, 18107 (2015).
[11] R. Süsstrunk and S. D. Huber, Proceedings of the National Academy of Sciences **113**, E4767 (2016).
[12] T. Ozawa, H. M. Price, A. Amo, N. Goldman, M. Hafezi, L. Lu, M. C. Rechtsman, D. Schuster, J. Simon, O. Zilberberg, and I. Carusotto, Rev. Mod. Phys. **91**, 015006 (2019).
[13] L. Lu, J. D. Joannopoulos, and M. Soljačić, Nature photonics **8**, 821 (2014).
[14] J. M. B. Lopes dos Santos, N. M. R. Peres, and A. H. Castro Neto, Phys. Rev. Lett. **99**, 256802 (2007).
[15] E. J. Mele, Phys. Rev. B **81**, 161405 (2010).
[16] G. Trambly de Laissardière, D. Mayou, and L. Magaud, Nano letters **10**, 804 (2010).
[17] S. Shallcross, S. Sharma, E. Kandelaki, and O. A. Pankratov, Phys. Rev. B **81**, 165105 (2010).
[18] E. Suárez Morell, J. D. Correa, P. Vargas, M. Pacheco, and Z. Barticevic, Phys. Rev. B **82**, 121407 (2010).
[19] R. Bistritzer and A. H. MacDonald, Proceedings of the National Academy of Sciences **108**, 12233 (2011).
[20] M. Kindermann and P. N. First, Phys. Rev. B **83**, 045425 (2011).
[21] L. Xian, S. Barraza-Lopez, and M. Y. Chou, Phys. Rev. B **84**, 075425 (2011).
[22] J. L. Dos Santos, N. Peres, and A. C. Neto, Physical Review B **86**, 155449 (2012).
[23] P. Moon and M. Koshino, Phys. Rev. B **85**, 195458 (2012).
[24] G. Trambly de Laissardière, D. Mayou, and L. Magaud, Phys. Rev. B **86**, 125413 (2012).
[25] P. Moon and M. Koshino, Phys. Rev. B **87**, 205404 (2013).
[26] Y. Cao, J. Y. Luo, V. Fatemi, S. Fang, J. D. Sanchez-Yamagishi, K. Watanabe, T. Taniguchi, E. Kaxiras, and P. Jarillo-Herrero, Phys. Rev. Lett. **117**, 116804 (2016).
[27] Y. Cao, V. Fatemi, S. Fang, K. Watanabe, T. Taniguchi, E. Kaxiras, and P. Jarillo-Herrero, Nature **556**, 43 (2018).
[28] W. Landgraf, S. Shallcross, K. Türschmann, D. Weckbecker, and O. Pankratov, Phys. Rev. B **87**, 075433 (2013).
[29] E. Suárez Morell, R. Vergara, M. Pacheco, L. Brey, and L. Chico, Phys. Rev. B **89**, 205405 (2014).
[30] E. S. Morell, P. Vargas, P. Häberle, S. A. Hevia, and L. Chico, Phys. Rev. B **91**, 035441 (2015).
[31] M. Pelc, E. S. Morell, L. Brey, and L. Chico, J. Phys. Chem. C **119**, 10076 (2015).
[32] M. Fleischmann, R. Gupta, D. Weckbecker, W. Landgraf, O. Pankratov, V. Meded, and S. Shallcross, Physical Review B **97**, 205128 (2018).
[33] J. Liu, J. Liu, and X. Dai, Physical Review B **99**, 155415 (2019).
[34] K. Wakabayashi, M. Fujita, H. Ajiki, and M. Sigrist, Phys. Rev. B **59**, 8271 (1999).
[35] M. Fujimoto, H. Koschke, and M. Koshino, Phys. Rev. B **101**, 041112 (2020).
[36] Y. Zhang, Y. Gao, and D. Xiao, Physical Review B **101**, 041410 (2020).
[37] Y. Su and S.-Z. Lin, Physical Review B **101**, 041113 (2020).
[38] D. J. Thouless, Phys. Rev. B **27**, 6083 (1983).
[39] T. Nakanishi and T. Ando, Journal of the Physical Society of Japan **70**, 1647 (2001).

[40] S. Uryu, Phys. Rev. B **69**, 075402 (2004).
[41] J. C. Slater and G. F. Koster, Phys. Rev. **94**, 1498 (1954).
[42] Y. Cao, V. Fatemi, A. Demir, S. Fang, S. L. Tomarken, J. Y. Luo, J. D. Sanchez-Yamagishi, K. Watanabe, T. Taniguchi, E. Kaxiras, *et al.*, Nature **556**, 80 (2018).
[43] N. N. Nam and M. Koshino, Physical Review B **96**, 075311 (2017).
[44] M. Koshino, N. F. Yuan, T. Koretsune, M. Ochi, K. Kuroki, and L. Fu, Physical Review X **8**, 031087 (2018).
[45] M. Koshino, New Journal of Physics **17**, 015014 (2015).
[46] M. Koshino and P. Moon, Journal of the Physical Society of Japan **84**, 121001 (2015).
[47] D. Weckbecker, S. Shallcross, M. Fleischmann, N. Ray, S. Sharma, and O. Pankratov, Physical Review B **93**, 035452 (2016).
[48] K. Uchida, S. Furuya, J.-I. Iwata, and A. Oshiyama, Phys. Rev. B **90**, 155451 (2014).
[49] M. M. van Wijk, A. Schuring, M. I. Katsnelson, and A. Fasolino, 2D Materials **2**, 034010 (2015).
[50] S. Dai, Y. Xiang, and D. J. Srolovitz, Nano letters **16**, 5923 (2016).
[51] S. K. Jain, V. Juričić, and G. T. Barkema, 2D Materials **4**, 015018 (2016).
[52] M. Koshino, N. F. Q. Yuan, T. Koretsune, M. Ochi, K. Kuroki, and L. Fu, Phys. Rev. X **8**, 031087 (2018).
[53] S. Carr, S. Fang, Z. Zhu, and E. Kaxiras, Physical Review Research **1**, 013001 (2019).
[54] M. Koshino and N. N. Nam, Physical Review B **101**, 195425 (2020).
[55] Y. Hatsugai and T. Fukui, Physical Review B **94**, 041102 (2016).
[56] M. Kindermann, B. Uchoa, and D. L. Miller, Phys. Rev. B **86**, 115415 (2012).
[57] J. R. Wallbank, A. A. Patel, M. Mucha-Kruczyński, A. K. Geim, and V. I. Fal'ko, Phys. Rev. B **87**, 245408 (2013).
[58] M. Mucha-Kruczyński, J. R. Wallbank, and V. I. Fal'ko, Phys. Rev. B **88**, 205418 (2013).
[59] J. Jung, A. Raoux, Z. Qiao, and A. H. MacDonald, Phys. Rev. B **89**, 205414 (2014).
[60] P. Moon and M. Koshino, Phys. Rev. B **90**, 155406 (2014).
[61] C. R. Dean, L. Wang, P. Maher, C. Forsythe, F. Ghahari, Y. Gao, J. Katoch, M. Ishigami, P. Moon, M. Koshino, *et al.*, Nature **497**, 598 (2013).
[62] L. Ponomarenko, R. Gorbachev, G. Yu, D. Elias, R. Jalil, A. Patel, A. Mishchenko, A. Mayorov, C. Woods, J. Wallbank, *et al.*, Nature **497**, 594 (2013).
[63] B. Hunt, J. D. Sanchez-Yamagishi, A. F. Young, M. Yankowitz, B. J. LeRoy, K. Watanabe, T. Taniguchi, P. Moon, M. Koshino, P. Jarillo-Herrero, *et al.*, Science **340**, 1427 (2013).
[64] G. Yu, R. Gorbachev, J. Tu, A. Kretinin, Y. Cao, R. Jalil, F. Withers, L. Ponomarenko, B. Piot, M. Potemski, *et al.*, Nature physics **10**, 525 (2014).
[65] F. Wu, T. Lovorn, E. Tutuc, and A. H. MacDonald, Physical review letters **121**, 026402 (2018).
[66] M. H. Naik and M. Jain, Physical review letters **121**, 266401 (2018).
[67] K. L. Seyler, P. Rivera, H. Yu, N. P. Wilson, E. L. Ray, D. G. Mandrus, J. Yan, W. Yao, and X. Xu, Nature **567**, 66 (2019).
[68] K. Tran, G. Moody, F. Wu, X. Lu, J. Choi, K. Kim, A. Rai, D. A. Sanchez, J. Quan, A. Singh, *et al.*, Nature **567**, 71 (2019).
[69] C. Jin, E. C. Regan, A. Yan, M. I. B. Utama, D. Wang, S. Zhao, Y. Qin, S. Yang, Z. Zheng, S. Shi, *et al.*, Nature **567**, 76 (2019).
[70] E. M. Alexeev, D. A. Ruiz-Tijerina, M. Danovich, M. J. Hamer, D. J. Terry, P. K. Nayak, S. Ahn, S. Pak, J. Lee, J. I. Sohn, *et al.*, Nature **567**, 81 (2019).

Appendix A: Sliding Chern number of a single valley

Here we prove the sliding Chern numbers of K and K' are equal due to the time reversal symmetry. The (spinless) continuum Hamiltonian for the low-angle TBG is written as

$$\mathcal{H}_\xi(\mathbf{k},\boldsymbol{\lambda}) = \begin{pmatrix} H_\xi^1(\mathbf{k}) & U_\xi^\dagger(\mathbf{k},\boldsymbol{\lambda}) \\ U_\xi(\mathbf{k},\boldsymbol{\lambda}) & H_\xi^2(\mathbf{k}) \end{pmatrix} \tag{A1}$$

where $\xi = K, K'$ is the valley index, $\boldsymbol{\lambda}$ is the sliding vector, H^l $(l = 1, 2)$ is the Hamiltonian for monolayer graphene and U is the interlayer coupling. The Hamiltonians for the opposite valleys are related by time reversal operation,

$$\mathcal{T}\mathcal{H}_K(\mathbf{k},\boldsymbol{\lambda})\mathcal{T}^\dagger = \mathcal{H}_{K'}(-\mathbf{k},\boldsymbol{\lambda}), \tag{A2}$$

where $\mathcal{T} = \mathcal{K}$ is the complex conjugation operator. Therefore its eigenvalues and Bloch wave functions follow

$$\begin{aligned} E_{K,n}(\mathbf{k},\boldsymbol{\lambda}) &= E_{K',n}(-\mathbf{k},\boldsymbol{\lambda}), \\ u_{K,n}(\mathbf{k},\boldsymbol{\lambda}) &= u^*_{K',n}(-\mathbf{k},\boldsymbol{\lambda}). \end{aligned} \tag{A3}$$

We define the sliding Chern numbers of a single valley as

$$C_{ij}^{(l)}(\xi) = \sum_{n=\text{ occupied}} \int_0^1 dk_j \int_0^1 d\lambda_i \Omega^\xi(k_j,\lambda_i) \tag{A4}$$

where

$$\Omega^\xi(k_j,\lambda_i) = i\left[\left\langle \frac{\partial u_\xi}{\partial \lambda_i}\middle|\frac{\partial u_\xi}{\partial k_j}\right\rangle - \left\langle \frac{\partial u_\xi}{\partial k_j}\middle|\frac{\partial u_\xi}{\partial \lambda_i}\right\rangle\right] \tag{A5}$$

is the Berry curvature in (k_j, λ_i) parameter space. From Eq.(A3) and Eq.(A5), the Berry curvatures of the opposite valleys are related by

$$\Omega^K(k_j, \lambda_i) = \Omega^{K'}(-k_j, \lambda_i), \tag{A6}$$

which finally leads to

$$C_{ij}^{(l)}(K) = C_{ij}^{(l)}(K'). \tag{A7}$$

Appendix B: Moiré edge states in other twist angles

In main text, we calculated the energy spectrum of the TBG ribbon with $\theta = 1.05°$ [Fig. 4], where we showed the emergence of the edge states is related by non-zero sliding Chern number. Actually the edge states exist in other twisted angles, as long as the gap remains opens at each k_y. Here we present the plots similar to Fig. 4 calculated for TBG ribbons of $\theta = 1.47°, 2.65°$ and $6.01°$ in Figs. 6, 7 and 8, respectively. In increasing the twist angle from $1.05°$, the moiré gap between the flat band and the excited band partially closes in some region of k_y. But still, we see the same number of the edge-state pumping in the gapped region, because the sliding Chern number remains unchanged in the gap.

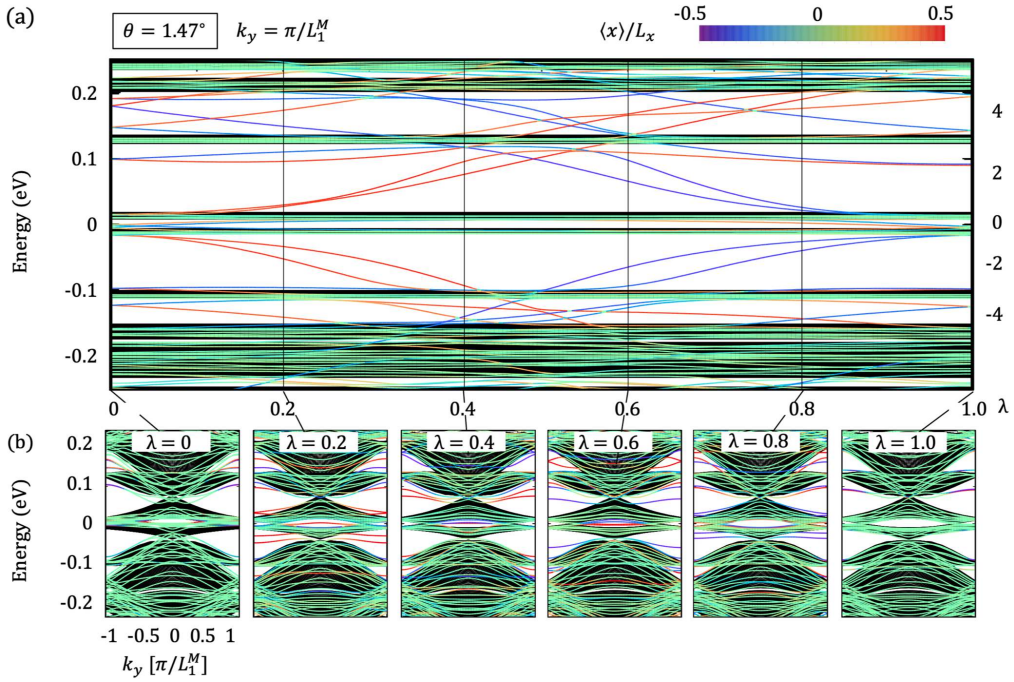

FIG. 6. Plot similar to Fig. 4 calculated for TBG ribbons of $\theta = 1.47^\circ$.

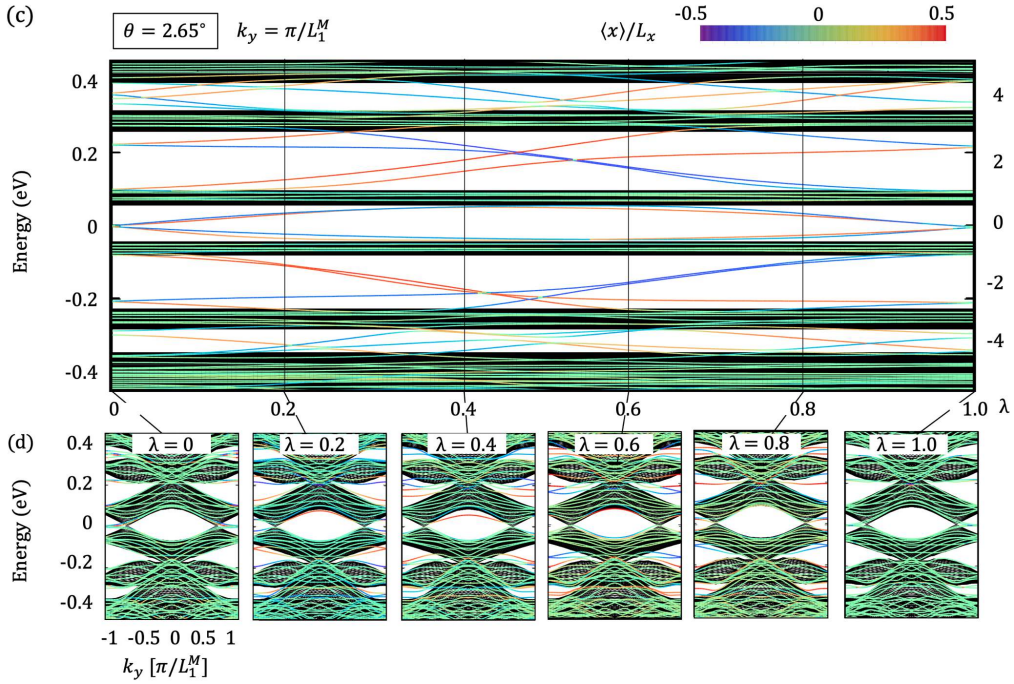

FIG. 7. Plot similar to Fig. 4 calculated for TBG ribbons of $\theta = 2.65^\circ$.

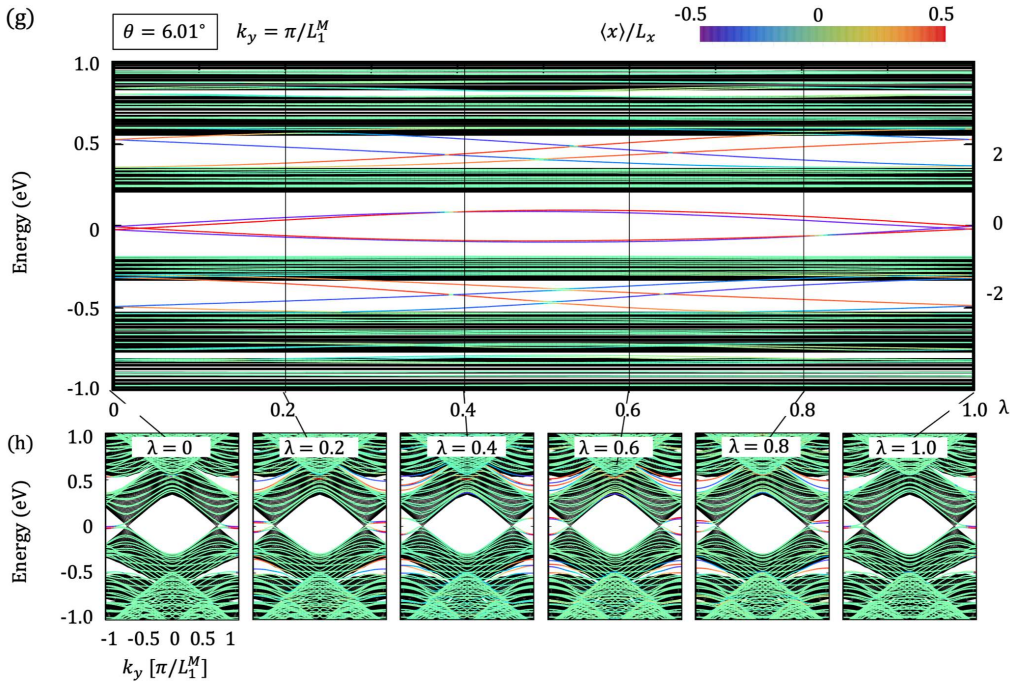

FIG. 8. Plot similar to Fig. 4 calculated for TBG ribbons of $\theta = 6.01^\circ$.